Thermal phase transition controlling electromagnetic wave absorption behavior of PAN fiber derived porous magnetic absorber

Yihan Zhao[1,2], Zhichao Lou[1,2,*], Qiuyi Wang[1,2], Yihua Wang[3], Wei Sun[1,2], and Yanjun Li[2,*]

[1] *Jiangsu Co-Innovation Center of Efficient Processing and Utilization of Forest Resources, Nanjing Forestry University, Nanjing 210037, China*
[2] *College of Materials Science and Engineering, Nanjing Forestry University, Nanjing 210037, China*
[3] *Forestry Bureau of Zixi County, Fuzhou 335300, Jiangxi Province, China*

ABSTRACT

The increasing excess electromagnetic wave (EMW) energies causes potential electromagnetic radiation pollution. It gives rise to more and more attention on designing environmentally friendly, efficient and suitable for large-scale industrial production of daily EMW absorbers. Carbon matrix composites modified with magnetic particles occupy the majority of these candidate absorbers. However, the preparation is still in its infancy. Here, we creatively mixed $Fe(acac)_3$ with polyacrylonitrile (PAN) spinning solution, and then prepared magnetic carbon-based composites by in-situ pyrolysis of the obtained electrospun fibers ($Fe(acac)_3$/PAN) at different temperatures. The SEM images display a fractured fibrous material with porous structure and uniform distribution of magnetic particles on the outer surface and inside. The XRD and XPS results indicate the composites consist of Fe_3O_4, Fe_3C and carbon matrix. Besides, the thermal phase transition occurs with the pyrolysis temperature increasing from 300 to 1000 °C, and the formed Fe_3O_4 reacts with the carbon matrix to form Fe_3C. As a result, the corresponding magnetic properties and electromagnetic properties improve. MCF-1000 exhibits enhanced EMW absorption performance with a minimum RL (RL_{min}) value of $- 29.27$ dB at a matching frequency (f_m) of 11.68 GHz, a matching thickness (t_m) as low as 1.50 mm, and an effective frequency bandwidth as broad as 4.50 GHz from 13.50 to 18.00 GHz at a fixed thickness as thin as 1.13 mm. Further investigations indicate that such good EMW absorption behavior is attributed to the optimal impedance matching and the weakened eddy current effect which are both benefited by the thermal phase transition effect. The results provide theoretical and practical experience for the industrial large-scale preparation of a kind of EMW absorbers.

Address correspondence to E-mail: zc-lou2015@njfu.edu.cn; nfcm2018@163.com

Springer

1 Introduction

With the development of information technology and electronic technology, various kinds of electronic equipment emerge one after another, which greatly facilitates people's daily production and life. However, the excess electromagnetic wave (EMW) energy is easy to cause electromagnetic radiation pollution, and seriously leads to a bewildering order in people's lives, abnormal operation of equipment and instruments, and even harms the ecological environment [1–3]. Finally, through the food chain, human health is affected, causing disease or cancer [4, 5]. Therefore, people pay more and more attention to the treatment of electromagnetic pollution. Electromagnetic shielding technology changes with each passing day, including EMW reflection and EMW absorption [6–9]. However, EMW reflection can hardly solve EMW radiation pollution, and sometimes even aggravate the problem. In contrast, EMW absorption can make EMW energy into heat or other energy and dissipate, and then reduce the EMW radiation energy to solve the problem of EMW radiation pollution [10–12]. Generally, EMW absorption is realized by EMW absorber. Dielectric loss [13] and magnetic loss [14] occur when EMWs enter an absorber. As a result, EMW energies are finally converted into energies in other forms. For an ideal EMW absorber, it is necessary to have the characteristics of light weight, thin matching thickness, wide effective absorption band and strong EMW absorption capacity [15–19].

EMW absorbers are usually magnetic conductive materials, which can effectively absorb EMWs through electromagnetic synergistic effect [20, 21]. Therefore, many studies have begun to construct magnetic conductive composites. Among these alternative absorbers, carbon-based composites have attracted much attention due to their excellent electrical conductivity, thermal stability, chemical stability, easy modification and lightweight, and controllable magnetism through the hybridization of magnetic components [22–24]. Iron containing materials such as Fe_3O_4 [25], Fe_2O_3 [26] and Fe_3C [27] are often used as magnetic components in carbon-based composites because of their abundant reserves on the earth, easy access, good biocompatibility and no harm to the environment and human body. In addition, in order to reduce the induced voltage of the incident EMWs and thus the eddy current loss, the nanometer hybridization inside the carbon matrix

was further studied [28]. At the same time, some carbon-based magnetic materials with special structural characteristics have been designed. For example, the porous structure can improve the conductivity of the absorber, meanwhile, it is conducive to the multiple reflection loss of the incident EMW inside the absorber [29, 30]; the shell-core structure is conducive to increasing the dipolar polarization effect of the absorber [31, 32]; and the other hetero structures are conducive to enhancing the interfacial polarization effect of the absorber [20, 33, 34]. In general, although these designs can effectively improve the EMW absorption behavior of an absorber, the corresponding preparation process is complex, involving many chemicals, the reaction conditions are harsh, the cost is high, and it is difficult to mass produce. Considering this, more efforts are needed to simplify the fabrication process of magnetic carbon-based composites with controllable structural characteristics and composition [35, 36].

Among candidate methods, thermal phase transition gives us useful inspiration [37, 38]. For example, the iron oxide in MSS is converted to Fe_3C at 750 °C, resulting in an enhanced EMW absorption behavior (a minimum reflection loss value of − 32.4 dB at 12 Hz). Similarly, the Fe_3N in the $Fe_3N@C$ composites is obtained by phase transition at 600 °C, thus enhancing the EMW absorption capacity (a minimum RL value of − 42.35 dB). Normally, carbon-based materials are prepared by the carbonization of thermosetting resins, carbon-rich polymers, coal and petroleum pitch at high temperature [39, 40]. However, it is difficult for the magnetic particles to be composited with the prepared carbon materials uniformly and effectively. A common method is to first build or acquire porous carbon precursor materials, such as foam [41] or biomass materials with interlinked conduits [42, 43], and then modify magnetic particles in the interior by impregnation, and finally obtain carbon-based magnetic composites by carbonization [44, 45]. However, there are some drawbacks to this approach. Firstly, it is difficult to accurately control the internal porosity and pore size of the obtained carbon precursor materials, and the pore size of the biomass material is also uneven, which leads to the uneven distribution of magnetic particles in the carbon precursor material. Secondly, the nanoparticles are easy to agglomerate, blocking the interior pores, so that the impregnation efficiency decreases gradually. As a solution, the Fe-containing

precursors (such as iron acetylacetonate (Fe(acac)$_3$), Fe(NO$_3$)$_3$, and other iron salts) are smaller than the magnetic nanoparticles and easy to be impregnated, so as to replace the magnetic nanoparticles to impregnate the porous carbon precursor materials [46]. For example, we try to impregnate wood blocks in Fe(acac)$_3$ solution, and then pyrolyze at 1000 °C to obtain magnetic carbonized wood, which has been proved to have good EMW absorption capacity [47]. However, due to the presence of the interior pressure generated by the compressed air inside the conduits, the complex impregnation method of vacuum/pressure cyclic impregnation is required. Besides, such method is time–cost and is only suitable for the porous carbon precursor materials with a small size [48]. In contrast, it has been proved to be an efficient method of adding iron salt precursor in the preparation of carbon precursor materials followed by in-situ pyrolysis. This method can ensure the uniform distribution of magnetic nanoparticles inside the carbon matrix and thus the corresponding good EMW absorption properties [49, 50].

Electrospinning is a common polymer preparation method which can realize large-scale production [51, 52]. It should be noted that other substances can be easily added into the spinning solution by a simple mixing method. As a result, composite spinning fiber can be realized. In this work, we creatively mixed Fe(acac)$_3$ with polyacrylonitrile (PAN) spinning solution, and then prepared magnetic carbon-based composites by in-situ pyrolysis at different temperatures. Through scanning electron microscope (SEM), X-ray diffraction (XRD) and X-ray photoelectron spectroscope (XPS), we finally determined that at different temperatures, the thermal phase transition of Fe(acac)$_3$/PAN composite fiber occurred. The electromagnetic properties of the pyrolyzed samples were analyzed by network vector analyzer. It was found that the thermal phase transition can effectively control the electromagnetic properties of the samples, and ultimately affect the corresponding EMW absorption properties. In addition, the absorption mechanism is investigated in depth. The results provide theoretical and practical experience for the preparation of a kind of EMW absorber with controllable thermal phase transition. At the same time, the preparation method designed in this work has the potential to realize large-scale industrial production of EMW absorbers.

2 Materials and methods

2.1 Materials

93 wt% PAN, 100 wt% dimethylformamide (DMF), and Fe(acac)$_3$ were obtained from Sigma-Aldrich Corp. St. Louis, MO USA.

2.2 Fiber preparation

6.5 g PAN was added into 50 mL DMF, and the mixture was stirred under ultrasonic at room temperature for 2 h, with a power of 320 W and a frequency of 40 kHz. Then, 0.84 g Fe(acac)$_3$ was added into 35 mL spinning solution containing 0.13 g/mL PAN in DMF under magnetic stirring for another 2 h under room temperature. As a result, Fe(acac)$_3$ containing PNA spinning DMF solution was prepared. The fibers were spun from solution through a wet method with a self-built spinning machine which was equipped with a spinneret. The corresponding hole diameter was 0.08 mm. The sprayed fibers were caught with tin cardboard and were further dried under isometric conditions at a temperature of 40 °C.

2.3 Fabrication of magnetic carbon-based composite

The obtained fibers were placed into a tube furnace. After the tube was filled with N$_2$ by air purging with N$_2$ flow for 30 min, the samples were heated to 220 °C at a heating rate of 5 °C/min, and the temperature was kept for 1 h at 220 °C. After that, the temperature was further increased to 300 °C at the same heating rate, and the temperature was also kept for 1 h. It is reported that Fe(acac)$_3$ can be decomposed into Fe$_3$O$_4$ nanoparticles at 300 °C. The obtained sample was named MCF-300. Then, the temperature was increased to 1000 °C at a heating rate of 5 °C/min and kept for another 1 h. The obtained sample was named MCF-1000. To be mentioned, after the carbonization process, the samples were cooled down to ambient temperature under N$_2$ protection.

2.4 Measurement of morphology, composition and magnetic properties

The morphologies of the obtained samples were observed by SEM (JSM-7800F). The XRD curves of the

samples were obtained by a Bruker D8 Advance powder X-ray diffractometer (Germany) with a 2θ scanning range from $10°$ to $80°$ using a Cu-Ka radiation source at 40 kV and 40 mA. The requested mass for each specimen is 200 mg. The XPS spectrum was measured in an AXIS UltraDLD (Shimadzu, Japan) using an Al Ka X-ray source at 150 W. A Lake Shore 7407 VSM from East Changing Technologies, Inc. was used to do the magnetic measurements. The requested mass for each sample was 10 mg.

2.5 Electromagnetic parameters measurement

Coaxial-line method was introduced to test the relative complex permittivities (ε', ε'') and relative complex permeabilities (μ', μ'') of the obtained samples. The testing frequency (f) is from 2 to 18 GHz, and the testing machine is Agilent PNA N5224A vector network analyzer. According to the manual, the samples were firstly mixed with paraffin wax with a mass fraction of 15% and pressed into a toroidal shape with an outer diameter of 7.0 mm and an inner diameter of 3.04 mm. The EMW absorption behavior of the samples was evaluated by the reflection loss (RL) according to the transmission line theory as below:

$$Z_{in} = Z_0(\mu_r/\varepsilon_r)^{1/2}\tan h\left[j(2\pi fd/c)(\mu_r\varepsilon_r)^{1/2}\right] \quad (1)$$

$$RL = 20\log_{10}|(Z_{in} - Z_0)/(Z_{in} + Z_0)| \quad (2)$$

where Z_0 and Z_{in} is the characteristic impedance of free space and the input impedance of the absorber, respectively. ε_r and μ_r is the relative complex permittivity and permeability, respectively. d and c is the sample thickness and the light velocity.

# 3 Results and discussion

3.1 Morphologies of the samples

Figure 1a displays the SEM images of Fe(acac)$_3$/PAN composite fibers with two different magnifications. It is obvious that the composite fibers are uniform in size and continuous in axial direction, exhibiting good flexibility. The width values of these fibers are also uniform, ranging from 2 to 3 μm. After carbonization, at the pyrolysis temperature of 300 °C and 1000 °C, the carbonized samples are all

fragmented (Fig. 1b and c), which is mainly due to the lack of previously reported solidification and drawing treatment before the pyrolysis process. Comparing the corresponding enlarged images in Fig. 1b(2) and c(2), we can find that the surface of MCF-300 is as smooth as that of the composite fiber in Fig. 1, while the surface of MCF-1000 is observed to be modified with some nano-sized particles. These particles are well-dispersed and occasionally small clusters appear. More importantly, porous structures can be clearly seen in the cross-section SEM images of pyrolyzed samples in Fig. 1d(1) and d(2), respectively, which are similar to the vessel and plant fiber cells in the biomass materials. MCF-1000 is different from MCF-300. The particles can be clearly observed on the cross-section of MCF-1000, which indicates that these particles are generated not only on the surface, but also inside the samples.

3.2 Components and fabrication mechanism of the samples

XRD can be used to analyze the crystallization of the samples [53]. Figure 2 shows the XRD curves of Fe(acac)$_3$/PAN composite fiber, MCF-300 and MCF-1000, respectively. It is obvious that the peak at $2\theta = \sim 20°$ which represents the diffraction peak for PAN, disappears as the pyrolysis temperature increases (from 300 to 1000 °C). And a new diffraction peak appears near $2\theta = \sim 26.5°$, representing the (111) plane of graphite crystalline carbon (JCPDS 75-0444). For MCF-300, the peaks at $2\theta = 30.96°$, 35.30°, 43.90°, 57.10° and 63.64°, corresponding to the (220), (311), (400), (511) and (440) planes of cubic Fe$_3$O$_4$ (JCPDS 19-629), indicates the formation of Fe$_3$O$_4$ inside the pyrolyzed samples at 300 °C. Further increasing the pyrolysis temperature to 1000 °C, additional diffraction peaks at $2\theta = 37.62°$, 42.78°, 43.68°, 44.68°, 45.70°, 48.52°, 49.04°, and 62.54° which represent the (210), (211), (102), (031), (131), (221), (122) and (114) planes of Fe$_3$C (JCPDS 35-0772), are observed for MCF-1000. The peaks at $2\theta = 30.96°$, 35.30°, 57.10° and 63.64° are still observed for MCF-1000, indicating the remaining of Fe$_3$O$_4$ after pyrolysis treatment.

Figure 3a displays the survey XPS curves for MCF-300 and MCF-1000, along with the corresponding high-resolution Fe2p, O1s and N1s spectrum in Fig. 3b–d, respectively. The percentage of Fe$_3$O$_4$ and Fe$_3$C in the final product for each sample are
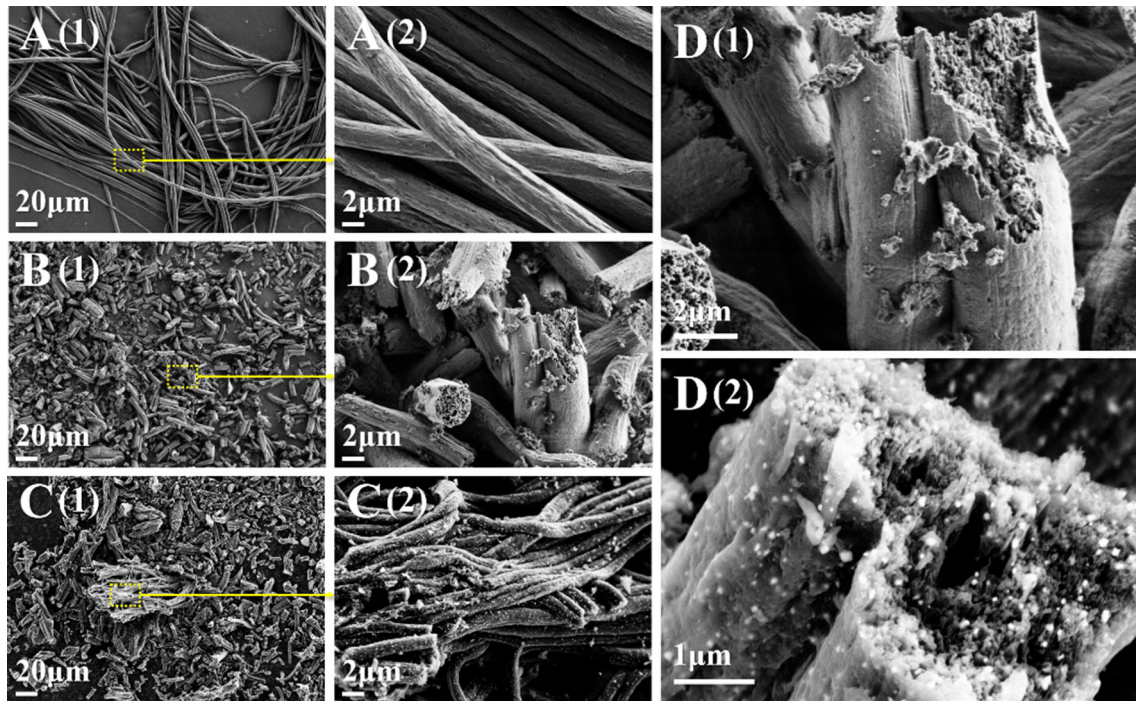
Fig. 1 SEM images of **a** Fe(acac)₃/PAN composite fiber, **b** MCF-300 and **c** MCF-1000 with different magnification. **d** SEM images of the cross-sections of MCF-300 and MCF-1000, respectively
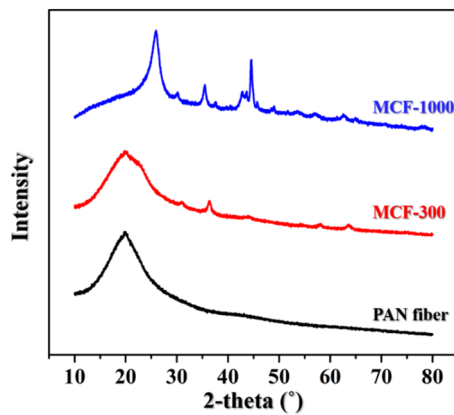

Fig. 2 XRD curves for Fe(acac)₃/PAN fibers (black), MCF-300 (red) and MCF-1000 (blue), respectively (Color figure online)

summarized in Table 1. As shown in Fig. 3a, MCF-300 consists of Fe, O and N while MCF-1000 has no N signal. Besides, the decreasing ratio of O/C from Fig. 3a indicates the carbonization of the obtained samples. As shown in Fig. 3b, the spectra of Fe2p of both samples exhibit double satellite signals at different binding energies. For MCF-300, the binding energies at ~ 711.0 and ~ 725.0 eV correspond to the characteristic doublet of $Fe2p_{3/2}$ and $Fe2p_{1/2}$ core-level electrons from Fe_3O_4. When pyrolyzed at 1000

°C, two more peaks at ~ 722.7 and ~ 709.0 eV are observed by deconvolution and Gaussian curve fitting, representing the characteristic doublet of $Fe2p_{3/2}$ and $Fe2p_{1/2}$ core-level electrons from Fe_3C. The peak at around ~ 532.5 eV in Fig. 3c is attributed to O1*s*, which is resolved by deconvolution and Gaussian curve fitting. It is obvious that both MCF-300 and MCF-1000 possess four signals at binding energies of 530.6 eV, 532.2 eV, 533.6 eV and 534.2 eV corresponding to the characteristic doublet from Fe_3O_4, O2, O3 and O4, respectively. The signal intensity ratio of O1s for Fe_3O_4 decreases with the increase of pyrolysis from 300 to 1000 °C, indicating the conversion from Fe_3O_4 to Fe_3C. Accordingly, the following two interactions possibly happen inside the sample during pyrolysis process as below:

$$Fe_3O_4 + C \rightarrow Fe_3C + 2O_2 \uparrow \qquad (3)$$

$$C + O_2 \rightarrow CO_2 \uparrow \qquad (4)$$

The gases (CO_2 and O_2) produced by the above reactions generate internal stress. They overflow from the sample together with the gas produced from the pyrolysis of PAN. As a result, pores are created inside the pyrolyzed sample as shown in Fig. 1d. The spectrum of N1*s* for MCF-300 in Fig. 3d exhibits
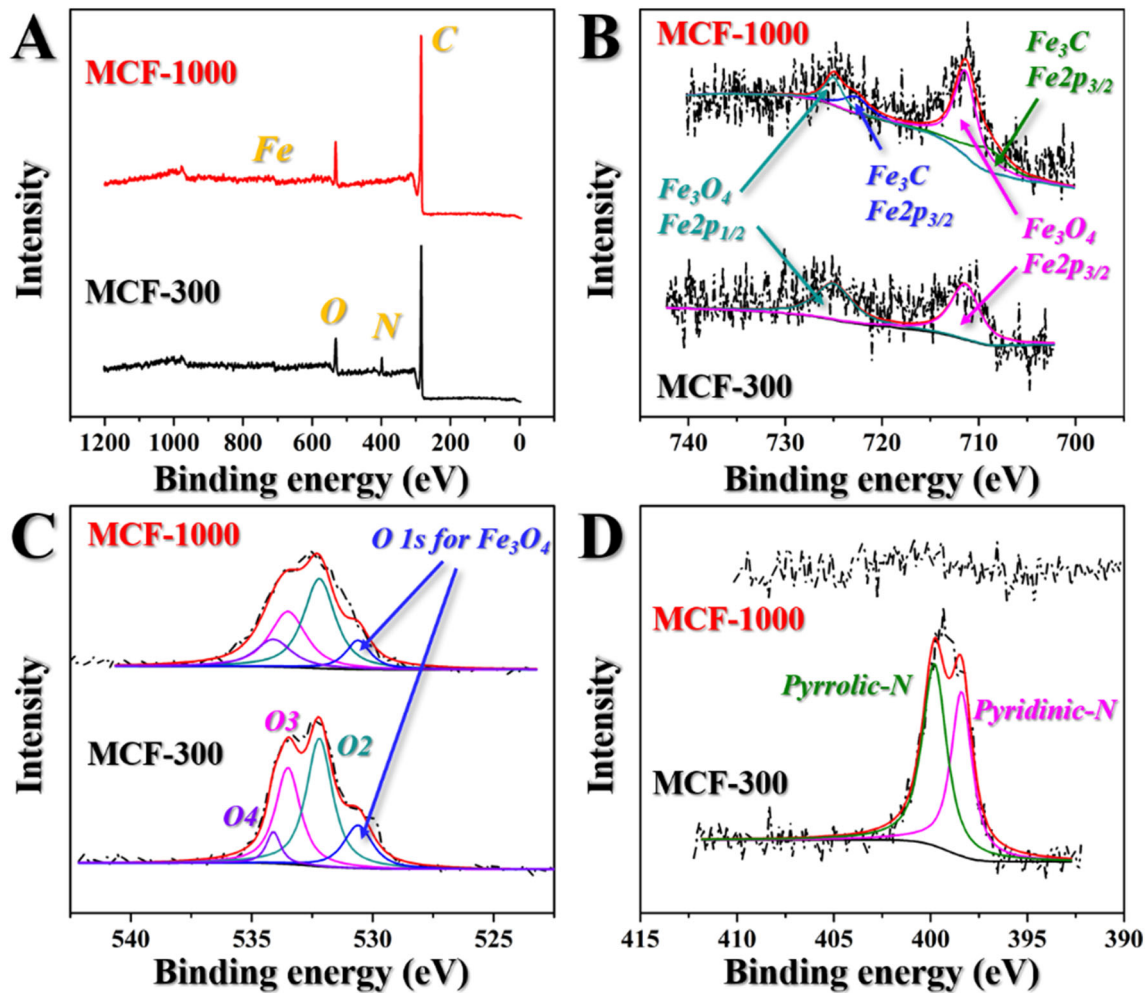
Fig. 3 a XPS curves for MCF-300 and MCF-1000, and their high-resolution XPS curves of **b** Fe2p, **c** O1s, **d** N1s, respectively

Table 1 The percentage of Fe_3O_4 and Fe_3C in the final product

|	Fe_3O_4 (%)	Fe_3C (%)
PAN fiber	0	0
MCF-300	13.9	0
MCF-1000	14.69	12.63

double satellite signals with two deconvoluted peaks at binding energies of 399.8 eV and 398.4 eV, corresponding to pyrrolic-N (H-N-(C)₂) and pyridinic-N (C-N = C). However, PAN is completely carbonized when heated to 1000 °C. As a result, N element is removed from the pyrolyzed samples in forms of light-weight gas molecules. And no N1s signal is observed for MCF-1000.

3.3 Magnetic properties of the samples

The magnetic properties of the prepared samples are measured by VSM as shown in Fig. 4. As could be seen, the saturation magnetization values (M_s) are 0.00, 7.08 and 23.64 emu/g for Fe(acac)₃/PAN fibers, MCF-300 and MCF-1000, respectively. The observed hysteretic behaviors for MCF-300 and MCF-1000 are attributed to the presence of incompletely carbonized PAN and generated Fe_3C. As we know, the presence of Fe_3C clusters as observed in Fig. 1d(2) can induce the increase of K_s [42]. Thus, the increased M_s value of the obtained samples should be attributed to the increased surface anisotropy (K_s) of the obtained samples. According to the following equation:

$$K_{eff} = K_b + (6/d)K_s \qquad (5)$$

K_s is positively related to the magnetocrystalline anisotropy (K_{eff}), where K_b is a constant about the
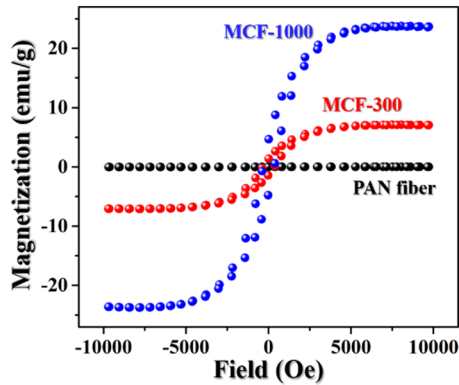
Fig. 4 VSM curves for PAN fiber, MCF-300 and MCF-1000, respectively

bulk anisotropy, d is the diameter of the modified Fe-containing particles (Fe_3O_4 or Fe_3C). As a result, the M_s value increases with the increasing temperature and with the presentation of the obtained Fe-containing particles on the surface of the fibers, according to Stoner-Wohlfarth theory:

$$M_s = (2K_{eff})/(\mu_0 H_c) \tag{6}$$

where μ_0 and H_c is the permeability constant and coercivity, respectively [54].

## 3.4 EMW absorption performances of the samples

Figure 5 displays the two-dimensional (2D) color fill image of RL values of MCF-300 and MCF-1000 with a filler loading rate of 30%, along with their corresponding 2D color fill image of $|Z_{in}/Z_0|$ values. As shown in Fig. 5a, all the obtained RL values at the frequency from 2 to 18 GHz with a coating thickness from 1 to 5 mm are larger than − 2.0 dB. Therefore, MCF-300 exhibits no effective EMW absorption performance. By comparison, MCF-1000 presents an effective absorption performance with a minimum RL (RL_{min}) value of − 29.27 dB at a matching frequency (f_m) of 11.68 GHz and a matching thickness (t_m) as low as 1.50 mm as shown in Fig. 5b. As we know, the $|RL|$ value larger than 10 dB indicates a 90% attenuation of incident EMW energies, indicating an effective absorption behavior. Accordingly, the effective absorption frequency bandwidth for MCF-1000 is as large as 4.50 GHz from 13.50 to 18.00 GHz at a fixed thickness as thin as 1.13 mm. Especially, we may see from Fig. 5b that partial RL_{min} values of MCF-1000 are lower than − 20 dB as circled by red lines, indicating

a $\geq$ 99% EMW energy attenuation. In addition, the corresponding bandwidth is as large as 9.09 GHz from 7.89 to 14.32 GHz and from 15.34 to 18.00 GHz, which is mainly concentrated in the higher frequency range. According to the transmission line theory, $|Z_{in}/Z_0|$ value of 1.00 implies the impedance matching and thus, no EMW reflection happens on the air/absorber interfaces. As a result, all the incident EMW energies enter the absorber and energy conversion occurs with maximum probability. Figure 5c displays 2D color fill image of the corresponding $|Z_{in}/Z_0|$ value of MCF-1000 with thickness ranging from 1.0 to 5.0 mm at frequencies of 2.0–18.0 GHz. It is calculated that the coverage ratio of $|Z_{in}/Z_0|$ value from 0.8 to 1.2 is 15.4%. In comparison, the corresponding calculated value for MCF-300 is as low as 9.7% as shown in Fig. 5d. This explains the phenomenon that MCF-1000 exhibits better EMW absorption performance than MCF-300. This can be attributed to the thermal phase transition from Fe_3O_4 to Fe_3C, indicating that Fe_3C is more conducive to EMW absorption. The EMW absorption performance of the carbon-/carbon fiber-based EMW absorbing materials is concluded in Table 2. It is obvious that MCF-1000 exhibits the best absorbing behavior among these absorbers.

The impedance matching theory can also be described as below:

$$Z_{in} = \sqrt{\frac{\mu_0}{\varepsilon_0}} \cdot \sqrt{\frac{\mu_r}{\varepsilon_r}} \tag{7}$$

where ε_0 and μ_0 is the relative complex permittivity and permeability of vacuum, respectively. Thus, the impedance matching is related to the ε_r and μ_r values of the absorber. In order to explore the mechanism of the EMW absorption behavior, the variation of electromagnetic parameters (complex permittivity and complex permeability) with frequency (2–18 GHz) is investigated in Fig. 6. As shown in Fig. 6A, the real parts of permittivity (ε') of MCF-1000, which represents its electronic storage capability, gradually decreases from 25.62 at 2.0 GHz to 15.25 at 18.0 GHz. However, the ε' value of MCF-300 varies lower than 5.00. Comparing MCF-300 with MCF-1000, the increase of ε' with the increase of pyrolysis temperature from 300 to 1000 °C is attributed to the further graphitization of carbon matrix at higher temperature and the phase transition from Fe_3O_4 to Fe_3C. Additionally, MCF-1000 possesses larger ε'' value of 2.57–
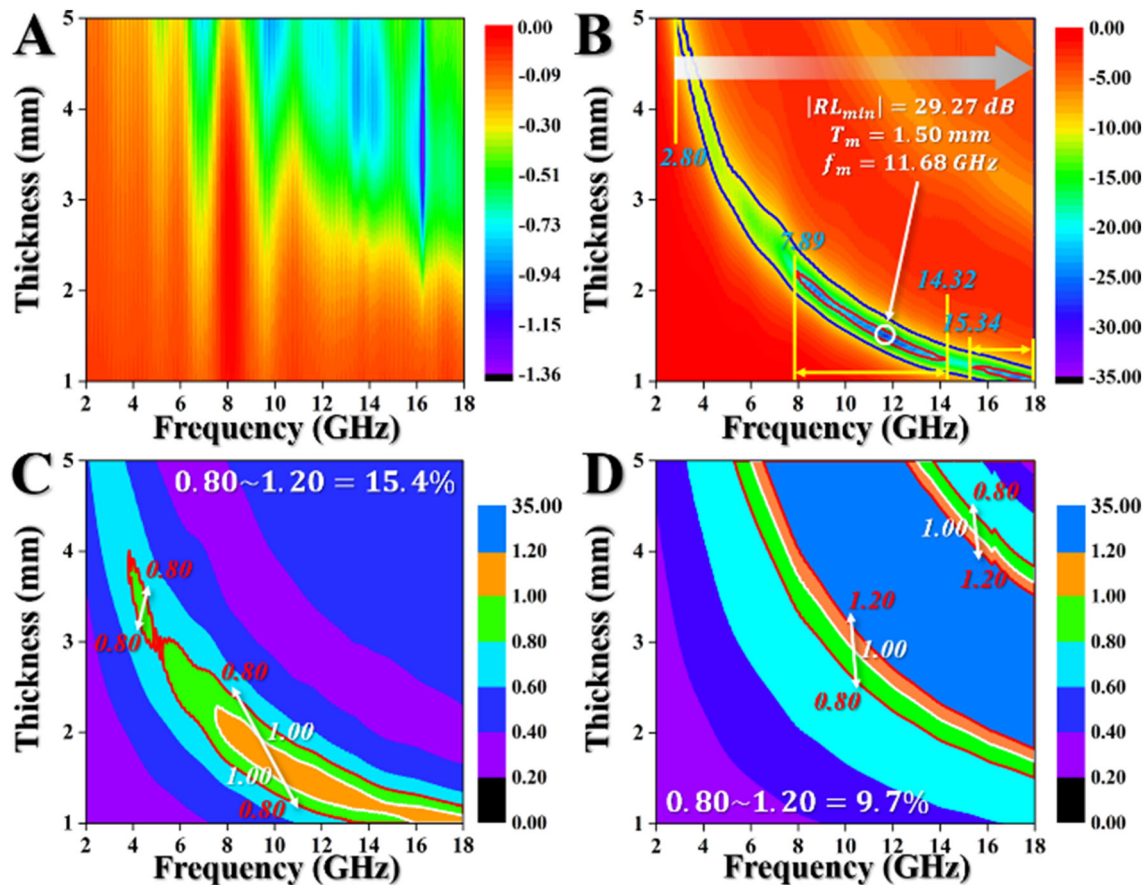
Fig. 5 **a**, **b** 2D color fill image of calculated RL values for MCF-300 and MCF-1000 with the thickness ranging from 1.0 to 5.0 mm and the frequency from 2.0 to 18.0 GHz. **c**, **d** 2D color fill image of calculated $|Z_{in}/Z_0|$ value for MCF-300 and MCF-1000, respectively (Color figure online)

Table 2 Comparison of the carbon-/carbon fiber-based EMW Absorber

| EMW absorber	Filler loading (wt%)	Thickness (mm)	Reflection loss (dB)	Bandwidth$_{max}$ (GHz)	Matching thickness (mm)	References
MCF-1000	15	1.5	− 29.27	4.5	1.13	Present work
BA30	30	1.6	− 26.1	3.1	1.5	[55]
CCF-1	40	1.0	− 12.1	4.6	1.0	[56]
CFF/epoxy	30	2.0	− 20.1	2.9	2.0	[57]
CNF-900	20	1.5	− 22.89	4.08	1.5	[58]
GSP-paraffin	35	1.6	− 21.9	4.72	1.6	[59]

*Bandwidth$_{max}$ = the largest effective absorption bandwidth at a fixed thickness

12.32 than that of MCF-300 as shown in Fig. 6b. It indicates that the internal rearrangement of electric dipole moments during the EMW propagation leads to its larger EMW energy loss capacity. To be mentioned, the observed frequency dispersion phenomena of ε' and ε'' is in favor of EMW dissipation.

Besides, the dielectric loss capacities of the prepared samples are estimated by dielectric loss tangent. And it can be calculated according to the following equation [60]:

$$\tan \delta_\varepsilon = \frac{\varepsilon''}{\varepsilon'} \tag{8}$$
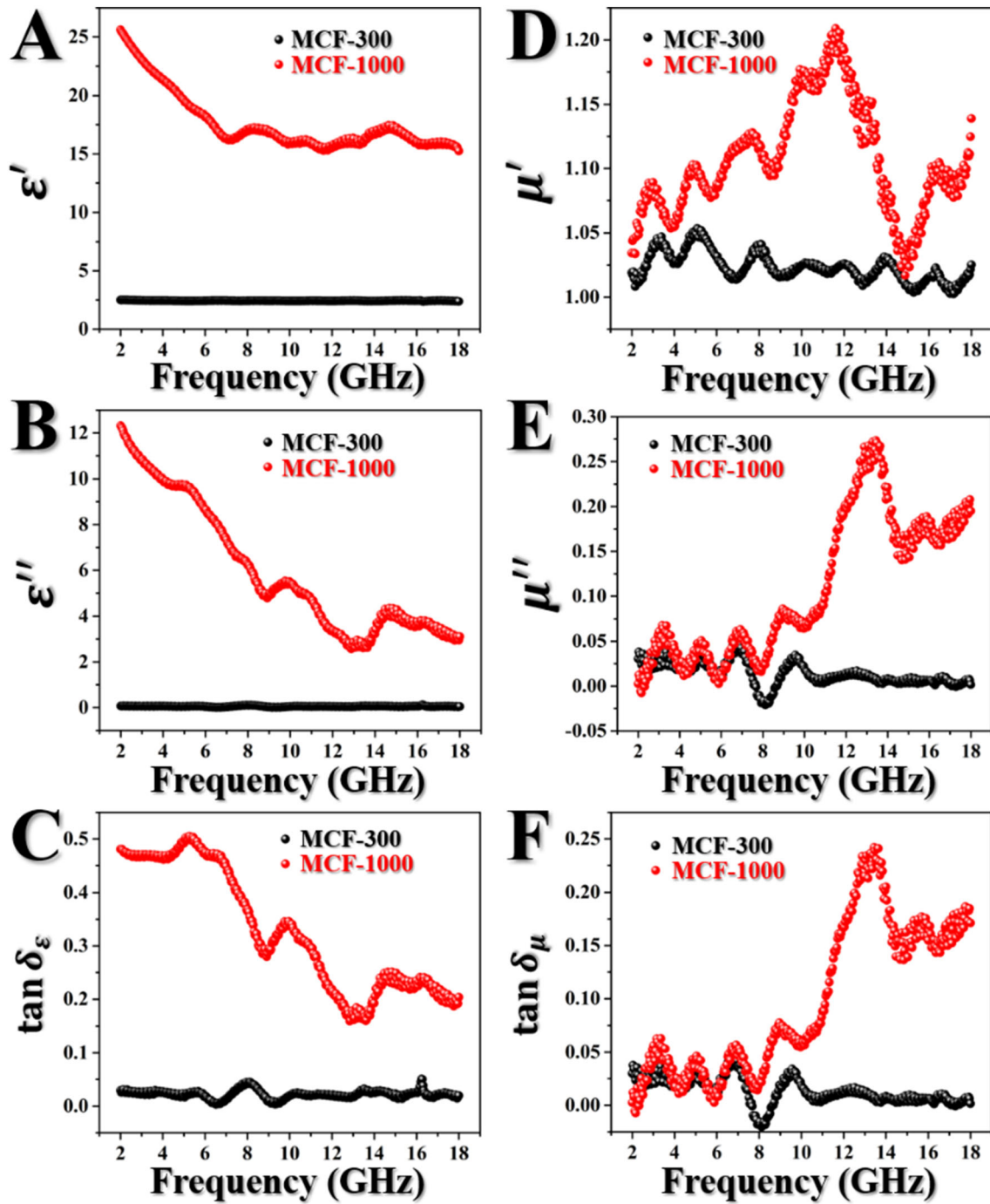
Fig. 6 **a**–**c** Dielectric parameters (real permittivity, imaginary permittivity and dielectric loss) of MCF-300 and MCF-1000, respectively. **d**–**f** Magnetic parameters (real permeability, imaginary permeability and magnetic loss) of MCF-300 and MCF-1000, respectively

where δ_ε is the lag phase of inductance field D relative to the external electric field. As shown in Fig. 6c, MCF-1000 possesses the highest $\tan\delta_\varepsilon$ value of 0.50 at 5.28 GHz while the highest $\tan\delta_\varepsilon$ value of MCF-300 is as low as 0.05 at 16.24 GHz. This result indicates that

MCF-1000 has larger capacities of converting the EMW to the energies in other forms.

Considering the presence of magnetic phases (Fe_3O_4 and Fe_3C) in the obtained samples, permeability (μ_r) is investigated. It represents the magnetic loss ability of the absorbers. Figure 6d and e display

the real part (μ') and the imaginary part (μ'') of permeability for MCF-300 and MCF-1000, respectively. As shown in Fig. 6d, MCF-1000 possesses the highest μ' value of 1.21 at 11.60 GHz which is larger than the highest μ' value of MCF-300 (1.05 at 5.08 GHz). This indicates that it has a large magnetic energy storage capacity. Meanwhile, MCF-1000 possesses the highest μ'' value of 0.27 at 13.44 GHz, indicating its largest EMW energy loss caused by the internal rearrangement of magnetic dipole moments under the electromagnetic field. Such magnetic loss ability from MCF-300 to MCF-1000 is consistent with the pyrolysis temperature increasing from 300 to 1000 °C. This is mainly due to the further graphitization of carbon matrix with the increase of pyrolysis temperature. At the same time, Fe_3O_4 formed at lower temperature (300 °C) reacts with the carbon matrix to generate Fe_3C with larger saturation magnetization, which in turn further improves the saturation magnetization of the obtained absorber (Fig. 4). Thus, better magnetic loss ability is achieved for MCF-1000 [61]. The magnetic loss capacities of the prepared samples are estimated by magnetic loss tangent which is calculated according to the following equation:

$$\tan \delta_\mu = \mu''/\mu' \tag{9}$$

The calculated results are shown in Fig. 6f, the variation of which is in accordance with that of μ'' value in Fig. 6e. In Fig. 6f, MCF-1000 shows a larger tangent value of 0.24 at 13.44 GHz than that of MCF-300. It is noted that the magnetic loss tangent is relatively lower than dielectric loss tangent, implying that the dielectric loss plays a dominant role in the attenuation of EMW energy.

It is noted that resonant peaks are observed in the ε'' curve in Fig. 6b, implying that multiple polarization relaxation processes may occur in the absorbers under alternating EM field. Thus, the dielectric loss mechanism is investigated by Debye relaxation theory described as below:

$$\left(\varepsilon' - \frac{\varepsilon_s + \varepsilon_\infty}{2}\right)^2 + (\varepsilon'')^2 = \left(\frac{\varepsilon_s - \varepsilon_\infty}{2}\right)^2 \tag{10}$$

where ε_s and ε_∞ is the static permittivity and relative permittivity in the higher frequency region, respectively [4]. According to the above equation, the plot of ε' versus ε'' should exhibit a Cole–Cole semicircle for a Debye relaxation process. The plots of ε' versus ε'' for MCF-300 and MCF-1000 are shown in Fig. 7a. It is

obvious that the plots shift to higher values from MCF-300 to MCF-1000 as the pyrolysis temperature increases from 300 to 1000 °C. It indicated that the contribution of Debye relaxation to dielectric loss enhances with the thermal phase transition from Fe_3O_4 to Fe_3C inside the obtained absorbers. Besides, compared with MCF-1000, MCF-300 exhibits no regular semicircle morphology, indicating that the corresponding multiple polarization relaxation is poor. By contraries, multiple regular Cole–Cole semicircles are observed for MCF-1000 in Fig. 7a. Especially, in the two electromagnetic frequency ranges of 7.89–14.32 GHz and 15.34–18.00 GHz, two regular Cole–Cole semicircles are observed in Fig. 7b, respectively. This corresponds to the part of RL values lower than − 20 dB. It indicates that the multiple polarization relaxation process plays an irreplaceable role in the EMW absorption behavior of MCF-1000. For MCF-1000, the formed Fe_3O_4/Fe_3C composites and carbon matrix act as polarized centers and induce polarization relaxations.

In general, the magnetic loss of EMWs in gigahertz range mainly derives from eddy current resonance, natural resonance and exchange resonance. Normally, eddy current resonance prevents the incident EMWs from entering the absorber, so it is unfavorable to the EMW absorption behavior of an absorber. The effect of eddy current resonance on the magnetic loss behavior of MCF-300 and MCF-1000 are investigated by the following equation:

$$C_0 = \mu''(\mu')^{-2} f^{-11} \tag{11}$$

The calculated C_0 values are shown in Fig. 8a. According to the criterion of skin effect theory, if the C_0 value remains a constant with the frequency, eddy
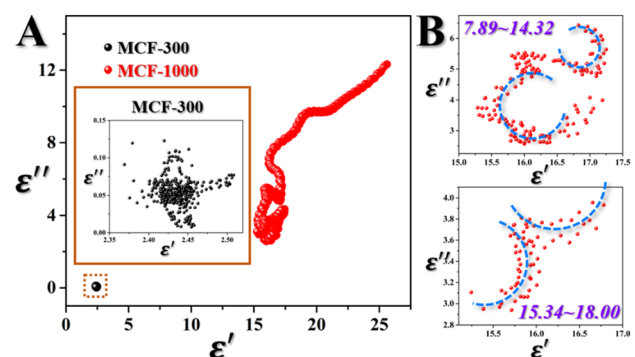
Fig. 7 a The plots of ε' versus ε'' for MCF-300 and MCF-1000, respectively. **b** The zoom-in ε' versus ε'' plots in the frequency ranges of 7.89–14.32 GHz and 15.34–18.00 GHz, respectively

current loss should be the only factor for magnetic loss. As shown in Fig. 8a, the C_0 value of MCF-1000 varies with the frequency, indicating that the eddy current loss can be neglected, and the natural resonance and exchange resonance should be the main contributors to the magnetic loss for MCF-1000. For MCF-300, we may see that the calculated C_0 value also varies with frequency from 2.0 to 12.0 GHz. But it nearly remains a constant at higher frequency range than 12.0 GHz, implying that the magnetic loss of MCF-300 at higher frequency is only attributed to the eddy current loss. In other words, the corresponding impedance matching is poor, and more EMW energy is reflected at the air/absorber interfaces due to the induced micro currents inside MCF-300 by eddy current effect. As a result, less EMW radiation penetrates the absorbers and the EMW absorption performance of MCF-300 is poor as shown in Fig. 5a.

The attenuation abilities of the samples are evaluated by the attenuation α value which is calculated as below:

$$\alpha = \frac{\sqrt{2}\pi f}{c}$$
$$* \sqrt{(\mu''\varepsilon'' - \mu'\varepsilon') + \sqrt{(\mu''\varepsilon'' - \mu'\varepsilon')^2 + (\mu'\varepsilon'' + \mu''\varepsilon')^2}}$$
(12)

As shown in Fig. 8b, MCF-1000 processes the larger α value, implying its larger attenuation ability than MCF-300. And thus, the corresponding stronger EMW absorption performance is achieved as shown in Fig. 5b.

4 Conclusions

Herein, a fractured fibrous material is prepared by in-situ pyrolysis of the as-prepared PAN/Fe(acac)$_3$ electrospinning fibers at different temperature. It has the porous structure and uniform distribution of Fe$_3$O$_4$/Fe$_3$C composites on the outer surface and inside. The components of the carbon-based magnetic composites and their corresponding electromagnetic properties are closely related to thermal phase transition. With the pyrolysis temperature increasing from 300 to 1000 °C, the formed Fe$_3$O$_4$ converts into Fe$_3$C. As a result, MCF-1000 which is obtained at 1000 °C exhibits enhanced EMW absorption performance with a minimum RL (RL_{min}) value of − 29.27 dB at a matching frequency (f_m) of 11.68 GHz, a matching thickness (t_m) as low as 1.50 mm, and an effective frequency bandwidth as broad as 4.50 GHz from 13.50 to 18.00 GHz at a fixed thickness as thin as 1.13 mm. Further investigations indicate that the thermal phase transition effect benefits the higher electromagnetic parameters, the optimal impedance matching and the weakened eddy current effect which lead to such good EMW absorption behavior. The results provide theoretical and practical experience for the industrial large-scale preparation of a kind of EMW absorbers.
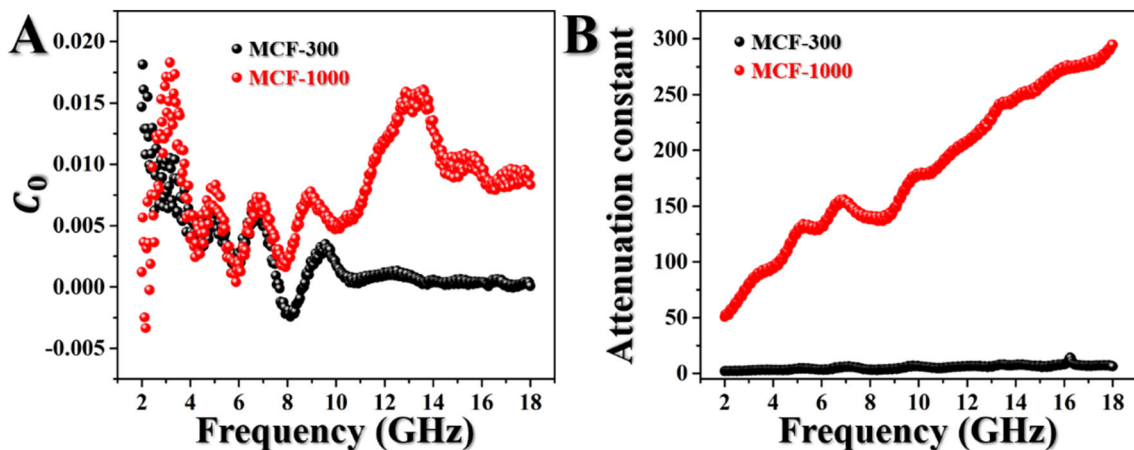
Fig. 8 **a** The calculated C_0 values of MCF-300 and MCF-1000, respectively. **b** Plots of α vs. frequency for MCF-300 and MCF-1000, respectively

Acknowledgements

References

1. D. Lan, Z. Zhao, Z. Gao, K. Kou, G. Wu, H. Wu, Porous high entropy alloys for electromagnetic wave absorption. J. Magn. Magn. Mater. **512**, 167065 (2020)

2. Z. Lou, W. Wang, C. Yuan, Y. Zhang, Y. Li, L. Yang, Fabrication of Fe/C composites as effective electromagnetic wave absorber by carbonization of pre-magnetized natural wood fibers. J. Bioresour. Bioprod. **4**(1), 43–50 (2019)

3. P. Liu, S. Gao, Y. Wang, Y. Huang, W. He, W. Huang, J. Luo, Carbon nanocages with N-doped carbon inner shell and Co/N-doped carbon outer shell as electromagnetic wave absorption materials. Chem. Eng. J. **381**, 122653 (2020)

4. W. Pei, W. Shang, C. Liang, X. Jiang, C. Huang, Q. Yong, Using lignin as the precursor to synthesize Fe_3O_4@lignin composite for preparing electromagnetic wave absorbing lignin-phenol-formaldehyde adhesive. Ind. Crop. Prod. **154**, 112638 (2020)

5. D. Fabien, The different sources of electromagnetic fields: dangers are not limited to physical health. Electromagn. Biol. Med. **39**, 166–175 (2020)

6. H. Lv, Y. Li, Z. Jia, L. Wang, X. Guo, B. Zhao, R. Zhang, Exceptionally porous three-dimensional architectural nanostructure derived from CNTs/graphene aerogel towards the ultra-wideband EM absorption. Compos. B **196**, 108122 (2020)

7. Z. Jia, C. Wang, A. Feng, P. Shi, C. Zhang, X. Liu, K. Wang, G. Wu, A low-dielectric decoration strategy to achieve absorption dominated electromagnetic shielding material. Compos. B **183**, 107690 (2020)

8. H. Lv, Z. Yang, H. Xu, L. Wang, R. Wu, An electrical switch-driven flexible electromagnetic absorber. Adv. Funct. Mater. **30**, 1907251 (2020)

9. Z. Lou, Q. Wang, Y. Zhang, X. Zhou, R. Li, J. Liu, Y. Li, H. Lv, In-situ formation of low-dimensional, magnetic core-shell nanocrystal for electromagnetic dissipation. Compos. B **214**, 108744 (2021)

10. Z. Shen, J. Chen, B. Li, G. Li, Z. Zhang, X. Hou, Recent progress in SiC nanowires as electromagnetic microwaves absorbing materials. J. Alloys Compd. **815**, 152388 (2020)

11. M. Cao, X. Wang, M. Zhang, J. Shu, W. Cao, H. Yang, X. Fang, J. Yuan, Electromagnetic response and energy conversion for functions and devices in low-dimensional materials. Adv. Funct. Mater. **29**, 1807398 (2019)

12. M.-S. Cao, Y.-Z. Cai, P. He, J.-C. Shu, W.-Q. Cao, J. Yuan, 2D MXenes: electromagnetic property for microwave absorption and electromagnetic interference shielding. Chem. Eng. J. **359**, 1265–1302 (2019)

13. Z. Gao, Z. Jia, K. Wang, X. Liu, L. Bi, G. Wu, Simultaneous enhancement of recoverable energy density and efficiency of lead-free relaxor-ferroelectric BNT-based ceramics. Chem. Eng. J. **402**, 125951 (2020)

14. B. Wen, H. Yang, Y. Lin, L. Wang, L. Ma, Y. Qiu, In situ anchoring carbon nanotubes on the Ni/C nanosheets with controllable thickness for boosting the electromagnetic waves absorption. Compos. A **138**, 106044 (2020)

15. X. Zeng, X. Cheng, R. Yu, G.D. Stucky, Electromagnetic microwave absorption theory and recent achievements in microwave absorbers. Carbon **168**, 606–623 (2020)

16. D.T. Chi, B.X. Khuyen, B.S. Tung, V.D. Lam, L.Y. Chen, Y. Lee, Progresses in metamaterials for advanced low-frequency perfect absorbers: a brief review. J. Electromagn. Wave Appl. **34**, 2251–2265 (2020)

17. Y. Wang, H. Xu, C. Wang, M. Wang, S. Wang, Research progress of electromagnetic metamaterial absorbers. Acta Phys. Sin. Chin. Ed. **69**, 134101 (2020)

18. S.K. Singh, M.J. Akhtar, K.K. Kar, Hierarchical carbon nanotube-coated carbon fiber: ultra lightweight, thin, and highly efficient microwave absorber. ACS Appl. Mater. Interfaces **10**, 24816–24828 (2018)

19. S.K. Singh, M.J. Akhtar, K.K. Kar, Synthesis of a lightweight nanocomposite based on polyaniline 3D hollow spheres integrated milled carbon fibers for efficient X-band microwave absorption. Ind. Eng. Chem. Res. **59**, 9076–9084 (2020)

20. Y. Wang, X. Di, X. Wu, X. Li, MOF-derived nanoporous carbon/Co/Co_3O_4/CNTs/RGO composite with hierarchical structure as a high-efficiency electromagnetic wave absorber. J. Alloys Compd. **846**, 156215 (2020)

21. Z. Lou, R. Li, J. Liu, Q. Wang, Y. Zhang, Y. Li, Used dye adsorbent derived N-doped magnetic carbon foam with enhanced electromagnetic wave absorption performance. J. Alloys Compd. **854**, 157286 (2021)

22. C. Wang, V. Murugadoss, J. Kong, Z. He, X. Mai, Q. Shao, Y. Chen, L. Guo, C. Liu, S. Angaiah, Z. Guo, Overview of carbon nanostructures and nanocomposites for electromagnetic wave shielding. Carbon **140**, 696–733 (2018)

23. M. Cao, C. Han, X. Wang, M. Zhang, Y. Zhang, J. Shu, H. Yang, X. Fang, J. Yuan, Graphene nanohybrids: excellent electromagnetic properties for the absorbing and shielding of electromagnetic waves. J. Mater. Chem. C **6**, 4586–4602 (2018)

24. C. Jia, T. Xia, Y. Ma, N. He, Z. Yu, Z. Lou, Y. Li, Fe_3O_4/α-Fe decorated porous carbon-based composites with adjustable electromagnetic wave absorption: impedance matching and loading rate. J. Alloys Compd. **858**, 157706 (2020)

25. Z. Lou, W. Wang, C. Yuan, Y. Zhang, Y. Li, L. Yang, Fabrication of Fe/C composites as effective electromagnetic wave absorber by carbonization of pre-magnetized natural wood fibers. J. Bioresour. Bioprod. **4**, 43–50 (2019)

26. B. Quan, G. Xu, D. Li, W. Liu, G. Ji, Y. Du, Incorporation of dielectric constituents to construct ternary heterojunction structures for high-efficiency electromagnetic response. J. Colloid Interface Sci. **498**, 161–169 (2017)

27. Y. Niu, X. Li, W. Dong, C. Zhang, K. Zhao, F. Wang, H. Wang, Synthesis of N-doped carbon with embedded Fe/Fe_3C particles for microwave absorption. J. Mater. Sci. **55**, 11970–11983 (2020)

28. Y.X. Gong, L. Zhen, J.T. Jiang, C.Y. Xu, W.Z. Shao, Preparation of CoFe alloy nanoparticles with tunable electromagnetic wave absorption performance. J. Magn. Magn. Mater. **321**, 3702–3705 (2009)

29. H. Zhao, Y. Cheng, H. Lv, G. Ji, Y. Du, A novel hierarchically porous magnetic carbon derived from biomass for strong lightweight microwave absorption. Carbon **142**, 245–253 (2019)

30. H. Zhao, Y. Cheng, W. Liu, L. Yang, B. Zhang, L.P. Wang, G. Ji, Z.J. Xu, Biomass-derived porous carbon-based nanostructures for microwave absorption. Nano-Micro Lett. **11**, 22 (2019)

31. H. Peng, X. Zhang, H. Yang, Z. Xiong, C. Liu, Y. Xie, Fabrication of core-shell nanoporous carbon@chiral polyschiff base iron(II) composites for high-performance electromagnetic wave attenuationin the low-frequency. J. Alloys Compd. **850**, 156816 (2021)

32. L. Chai, Y. Wang, N. Zhou, Y. Du, X. Zeng, S. Zhou, Q. He, G. Wu, In-situ growth of core-shell $ZnFe_2O_4$ @ porous hollow carbon microspheres as an efficient microwave absorber. J. Colloid Interface Sci. **581**, 475–484 (2021)

33. Y. Cheng, Y. Zhao, H. Zhao, H. Lv, X. Qi, J. Cao, G. Ji, Y. Du, Engineering morphology configurations of hierarchical flower-like MoSe2 spheres enable excellent low-frequency and selective microwave response properties. Chem. Eng. J. **372**, 390–398 (2019)

34. Y. Cheng, J. Cao, H. Lv, H. Zhao, Y. Zhao, G. Ji, In situ regulating aspect ratio of bamboo-like CNTs via Co_xNi_{1-x}-

catalyzed growth to pursue superior microwave attenuation in X-band. Inorg. Chem. Front. **6**, 309–316 (2019)

35. W. Chu, C. Tian, Y. Wang, J. Chu, Z. Li, Y. Du, X. Han, Performance vs convenience of magnetic carbon-metal nanocomposites: a low-cost and facile citrate-derived strategy for Feco alloy/carbon composites with high-performance microwave absorption. Comment. Inorg. Chem. **37**, 301–326 (2017)

36. M. Zhu, G. Diao, Review on the progress in synthesis and application of magnetic carbon nanocomposites. Nanoscale **3**, 2748 (2011)

37. X. Zhang, J. Li, B. He, S. Yang, Y. Li, D. Chen, Y. Li, Y. Peng, Phase transformation and carbon precipitation of coal fly ash magnetospheres during a CVD process for microwave adsorption. Ceram. Int. **45**, 18980–18981 (2019)

38. X. Cui, X. Liang, W. Liu, W. Gu, G. Ji, Y. Du, Stable microwave absorber derived from 1D customized heterogeneous structures of $Fe_3N@C$. Chem. Eng. J. **381**, 122589 (2020)

39. Z. Zhang, Z. Dong, X. Wang, Y. Dai, X. Cao, Y. Wang, R. Hua, H. Feng, J. Chen, Y. Liu, B. Hu, X. Wang, Synthesis of ultralight phosphorylated carbon aerogel for efficient removal of U(VI): batch and fixed-bed column studies. Chem. Eng. J. **370**, 1376–1387 (2019)

40. C. Chen, E.B. Kennel, A.H. Stiller, P.G. Stansberry, J.W. Zondlo, Carbon foam derived from various precursors. Carbon **44**, 1535–1543 (2006)

41. Y. Zhao, Y. Zhang, R. Li, Z. Wang, Z. Lou, Y. Li, Facile synthesis of ultralight and porous melamine-formaldehyde (MF) resin-derived magnetic graphite-like C_3N_4/carbon foam with electromagnetic wave absorption behavior. Curr. Comput.-Aided Drug Des. **10**, 656 (2020)

42. Z. Lou, H. Han, M. Zhou, J. Han, J. Cai, C. Huang, J. Zou, X. Zhou, H. Zhou, Z. Sun, Synthesis of magnetic wood with excellent and tunable electromagnetic wave-absorbing properties by a facile vacuum/pressure impregnation method. ACS Sustain. Chem. Eng. **6**, 1000–1008 (2018)

43. Z. Lou, J. Sun, H. Lu, J. Cai, J. Zou, X. Li, Z. Sun, H. He, Fabrication of magnetic wood and its magnetic and electromagnetic wave absorption properties. J. For. Eng. **2**, 24–29 (2017)

44. Z. Li, H. Lin, S. Ding, H. Ling, T. Wang, Z. Miao, M. Zhang, A. Meng, Q. Li, Synthesis and enhanced electromagnetic wave absorption performances of $Fe_3O_4@C$ decorated walnut shell-derived porous carbon. Carbon **167**, 148–159 (2020)

45. R. Li, Z. Lou, S. Gu, Q. Wang, J. Liu, Y. Li, Preparation of magnetic carbon with microwave absorption property using bamboo powder. J. For. Eng. **6**, 120–127 (2021)

46. J. Xiao, R. Hu, G. Chen, B. Xing, Facile synthesis of multifunctional bone biochar composites decorated with Fe/Mn oxide micro-nanoparticles: physicochemical properties, heavy

metals sorption behavior and mechanism. J. Hazard. Mater. **399**, 123067 (2020)

47. Z. Lou, Y. Li, H. Han, H. Ma, L. Wang, J. Cai, L. Yang, C. Yuan, J. Zou, Synthesis of porous 3D Fe/C composites from waste wood with tunable and excellent electromagnetic wave absorption performance. ACS Sustain. Chem. Eng. **6**, 15598–15607 (2018)

48. Z. Lou, C. Yuan, Y. Zhang, Y. Li, J. Cai, L. Yang, W. Wang, H. Han, J. Zou, Synthesis of porous carbon matrix with inlaid Fe_3C/Fe_3O_4 micro-particles as an effective electromagnetic wave absorber from natural wood shavings. J. Alloys Compd. **775**, 800–809 (2019)

49. H. Han, Z. Lou, P. Wang, Q. Wang, R. Li, Y. Zhang, Y. Li, Synthesis of ultralight and porous magnetic $g-C_3N_4/g$-carbon foams with excellent electromagnetic Wave (EMW) absorption performance and their application as a reinforcing agent for 3D printing EMW absorbers. Ind. Eng. Chem. Res. **59**, 7633–7645 (2020)

50. Z. Lou, R. Li, P. Wang, Y. Zhang, B. Chen, C. Huang, C. Wang, H. Han, Y. Li, Phenolic foam-derived magnetic carbon foams (MCFs) with tunable electromagnetic wave absorption behavior. Chem. Eng. J. **391**, 123571 (2020)

51. W. Huang, Z. Tong, R. Wang, Z. Liao, Y. Bi, Y. Chen, M. Ma, P. Lyu, Y. Ma, A review on electrospinning nanofibers in the field of microwave absorption. Ceram. Int. **46**, 26441–26453 (2020)

52. Y. Huo, K. Zhao, Z. Xu, Y. Tang, Electrospinning synthesis of SiC/carbon hybrid nanofibers with satisfactory electromagnetic wave absorption performance. J. Alloys Compd. **815**, 152458 (2020)

53. Z. Lou, T. Yuan, Q. Wang, X. Wu, S. Hu, X. Hao, X. Liu, Y. Li, Fabrication of crack-free flattened bamboo and its macro-/micro-morphological and mechanical properties. J. Renew. Mater. **9**(5), 959–977 (2021)

54. C.R. Vestal, Z.J. Zhang, Atom transfer radical polymerization synthesis and magnetic characterization of $MnFe_2O_4/$

polystyrene core/shell nanoparticles. J. Am. Chem. Soc. **124**, 14312–14313 (2002)

55. S.K. Singh, M.J. Akhtar, K.K. Kar, Impact of Al_2O_3, TiO_2, ZnO and $BaTiO_3$ on the microwave absorption properties of exfoliated graphite/epoxy composites at X-band frequencies. Compos. B **167**, 135–146 (2019)

56. G. Wu, Z. Jia, X. Zhou, G. Nie, H. Lv, Interlayer controllable of hierarchical $MWCNTs@C@FexOy$ cross-linked composite with wideband electromagnetic absorption performance. Compos. A **128**, 105687 (2020)

57. S.K. Singh, H. Prakash, M.J. Akhtar, K.K. Kar, Lightweight and high-performance microwave absorbing heteroatom-doped carbon derived from chicken feather fibers. ACS Sustain. Chem. Eng. **6**, 5381–5393 (2018)

58. W. Gua, J. Lv, B. Quan, X. Liang, B. Zhang, G. Ji, Achieving MOF-derived one-dimensional porous ZnO/C nanofiber with lightweight and enhanced microwave response by an electrospinning method. J. Alloys Compd. **806**, 983–991 (2019)

59. B. Quan, W. Liu, G. Xu, G. Ji, Y. Du, Nano sulfur particles decorated bi-lamella composites for superior electromagnetic wave absorption. J. Colloid Interface Sci. **543**, 138–146 (2019)

60. P. Liu, V.M.H. Ng, Z. Yao, J. Zhou, Y. Lei, Z. Yang, H. Lv, L.B. Kong, Facile synthesis and hierarchical assembly of flowerlike NiO structures with enhanced dielectric and microwave absorption properties. ACS Appl. Mater. Interfaces **9**, 16404–16416 (2017)

61. B. Lu, H. Huang, X.L. Dong, X.F. Zhang, J.P. Lei, J.P. Sun, C. Dong, Influence of alloy components on electromagnetic characteristics of core/shell-type Fe-Ni nanoparticles. J. Appl. Phys. **104**, 114313 (2008)

Publisher's Note Springer Nature remains neutral with regard to jurisdictional claims in published maps and institutional affiliations.